Journal of Industrial and Engineering Chemistry 92 (2020) 131–144

Contents lists available at ScienceDirect

Journal of Industrial and Engineering Chemistry

journal homepage: www.elsevier.com/locate/jiec

Understanding porous structure of SBA-15 upon pseudomorphic transformation into MCM-41: Non-direct investigation by carbon replication

Rafał Janus[a,b,*], Mariusz Wądrzyk[a,b], Marek Lewandowski[a,b], Piotr Natkański[c], Piotr Łątka[c], Piotr Kuśtrowski[c]

[a] AGH University of Science and Technology, Faculty of Energy and Fuels, al. A. Mickiewicza 30, 30-059 Kraków, Poland
[b] AGH University of Science and Technology, AGH Centre of Energy, ul. Czarnowiejska 36, 30-054 Kraków, Poland
[c] Jagiellonian University, Faculty of Chemistry, ul. Gronostajowa 2, 30-387 Kraków, Poland

ARTICLE INFO

Article history:
Received 13 July 2020
Received in revised form 12 August 2020
Accepted 30 August 2020
Available online 7 September 2020

Keywords:
Pseudomorphic transformation
Bimodal silica
Mesoporous sieves
Nanocasting
SBA-15
Carbon replicas

ABSTRACT

A series of mesoporous silicas with bimodal porosity combining the features of broad-mesoporous SBA-15 and narrow-mesoporous MCM-41 was synthesized by the pseudomorphic transformation of SBA-15. The pore size of the MCM-41-like fraction was adjusted using different quaternary ammonium salts, while the degree of pseudomorphic transformation was tuned by the alkalinity of the mother-silica dissolving agent. The produced silicas were applied as hard templates for the synthesis of carbon replicas by nanocasting. The mechanism of pseudomorphic transformation of mesoporous silica was for the first time investigated non-directly, employing the strategy of inverse carbon nanoreplication followed by comprehensive study of the textural and structural parameters of replicas with regard to silica matrices. It was found that the conversion of SBA-15 into MCM-41 occurs simultaneously throughout the entire particle's body according to the mechanism of *homogeneous pseudomorphic transformation*. It was evidenced that the strategy of inverse carbon replication could be successfully employed as an ingenious tool for non-direct investigation of suchlike silica transformations towards hierarchical porous systems. Furthermore, the unique bimodal mesoporosity of the carbons obtained from SBA-15 partially transformed into MCM-41 opens a possibility for their application in a variety of purposes, mainly in catalysis and adsorption.

Introduction

The synthesis of so-called *low bulk density silica* assisted by cationic surfactants was reported for the first time by Chiola et al., who received the patent for the procedure of its production in 1971 [1]. The material was devised as an intermediate in the manufacturing of luminescent materials (phosphors) based on metal orthosilicates. Unfortunately, since no meticulous physico-chemical characterization (particularly in terms of the textural parameters) was provided, the developed silica remained unnoticed by a broader scientific audience over the next two decades. In 1997 Di Renzo et al. [2] showed that the *low bulk density silica* was, in fact, a mesoporous material with a curious, long-range ordering of homogeneous, longitudinally oriented tubular pores, resembling in the cross-section the array of *honeycomb*, typical of MCM-41. Before, in 1992, the researchers from Mobil Research and Development Corporation, inspired by the previous patents by Beck et al. [3,4] carried out a successful synthesis of ordered mesoporous silica materials (OMS) by calcination of a siliceous solid precipitated in a presence of quaternary ammonium salt [5,6]. Therein, the authors elucidated the mechanism of the formation of OMS structures, called *liquid-crystal templating* (LCT). A hydrolyzing silica source introduced to a medium containing a liquid crystalline array undergoes self-assembly precipitation around supramolecular packets serving as a *structure directing agent* (SDA). After removal of SDA (most often by calcination), the structure of the liberated, pure silica retains the spatial arrangement of the SDA packets [5–7]. This seminal research became a milestone in developing a field of materials science concerned on the self-assembly synthesis of advanced nanoporous solids with a long-range ordering [8,9]. Later, the in-depth study on the mechanism of formation of MCM-41 showed that, in fact, the micelles and

* Corresponding author.
E-mail address: rjanus@agh.edu.pl (R. Janus).

https://doi.org/10.1016/j.jiec.2020.08.032

micellar liquid crystals are formed when silica source hydrolyzes and the ion pairs of silicate-quaternary ammonium salt assemble themself. This upgraded mechanism is known as *cooperative self-assembly process* [10].

Since the discovery of the LCT mechanism, the study on the OMS have been evolved in the following aspects: (i) controlled synthesis of new predetermined structures with the use of a variety of surfactants serving as SDAs, and (optionally) applying swelling agents and/or co-solvents, which govern the spatial array of the liquid crystal assemblies, (ii) modification of their surface and tailoring of their textural parameters and/or particles morphology, and ultimately (iii) testing in numerous applications [11–13]. An essential advantage of the OMS is mesoporosity, which breakthroughs the inherent mass transfer limitations within smaller pores of solids commonly used in adsorption and catalytic applications (viz. zeolites and activated carbons). Considering additionally other beneficial features of the OMS, including (i) large specific surface area, (ii) high pore volume, (iii) unique, highly ordered pore structure with a long-range arrangement, and (iv) surface susceptibility to facile modification resulting in a great application potential, it should not be surprising still increasing interest in research into this group of materials.

The OMS have been tested in catalysis (including photo- and biocatalysis) [12,14–26], adsorption, membrane separation, and nanofiltration [27–35], chromatography (as a stationary phase) [36–40], life science (as drug delivery carriers and antiseptic materials) [41–46], biotechnology (biomolecules immobilization) [47–49], sensor technologies (in devices for monitoring of relative humidity, pH, pesticide concentrations, and detection of gases) [50,51], as well as energy conversion and storage (sunlight conversion, electrode materials for batteries, supercapacitors) [52–56]. Furthermore, the OMS are very useful in development of new advanced nanoporous materials, for instance, in a role of matrices (*hard templates*) used in a synthesis of inverse carbon and polymer replicas [57–62], as well as ordered mesoporous metal oxides [63–65] by nanocasting.

One of possible methods used in a post-synthetic modification of porous silicas is *pseudomorphic transformation* (PT) [66]. This approach, somewhat similar to spontaneous pseudomorphism of minerals in nature, is based on transformation one porous silica into another, usually characterized by a higher ordering at the retained grain morphology. Typically, PT involves partial dissolution (leaching) of the silica walls of the mother material (usually employing a strongly alkaline medium) followed by reconstruction (re-condensation) of SiO_2 around packets of self-assembled SDA micelles (mostly the quaternary ammonium halides/hydroxides) introduced into the pore system [66–72]. A careful adjustment of PT conditions sometimes results in partial retaining features of the original meso- and macropores system. Therefore, the resulting material could exhibit either the presence of a portion of unaltered pores of the original silica accompanied by a portion of newly formed smaller pores emerging in the place of the SDA micelles removed from the re-condensed silica (partial PT) or possess solely the newly evolved porosity replacing that original one (total PT). The materials produced by the partial PT with tunable bimodal mesoporosity are excellent candidates for a model study on mechanisms of gas adsorption–desorption phenomena as well as molecule diffusion within the constricted pore system. Furthermore, the bimodal silicas may be interesting materials for shape-selective processes, including catalytic reactions (so-called *ship in a bottle* synthesis), and the *size-exclusion* membrane separation processes [69,70].

It is well-documented that both degree of transformation and quality of the ultimate material after PT (i.e. in terms of morphology and pore structure) are affected by the following essential factors: (i) features of the starting silica (pore size and volume, and wall thickness, i.e. too thick silica walls may prevent their depth penetration by a dissolving agent), (ii) pH of the mother solution, (iii) a type of applied SDA (i.e. commonly either *N,N,N*-trimethylalkylammonium hydroxide solution or a mixture of NaOH and *N,N,N*-trimethylalkylammonium salt), (iv) optional utilizing of a swelling agent, (v) duration and temperature of the dissolution and re-condensation processes, (vi) a method selected for removal of the SDA. Combination of PT with simultaneous functionalization also influences the quality of the ultimate product [67–69,71–76].

Although the general principles of PT mechanism have been explained, many issues still remain unclarified [66,69,70,73–75]. Heretofore, three hypothetical mechanisms of PT were proposed, as follows: (i) *core–shell mechanism*, assuming a progress of transformation from outside to a depth of grain, (ii) *reverse core–shell mechanism*, i.e. the PT undergoes from a core to outside of the particle, and (iii) *homogeneous transformation* within a whole pore system of SiO_2 particle [73,74]. Noteworthy, recent studies on PT have shown that the latter pathway seems to be the most likely, regardless of the type of starting porous silica [67–69,72,74,75], although no conclusive evidence has been provided as far.

As we have shown in our previous reports on the inverse carbon replication of SBA-15, employing the wet method of precipitation polycondensation of furfuryl alcohol (FA) in a water slurry of SiO_2 results in covering of its entire available internal and external surface by the formed poly(furfuryl alcohol) (PFA). When a sufficient amount of monomer is provided, the bulky PFA fills the pore interior without major incoherencies in the pore-filling bulk [32,59,60,77,78]. Consequently, the PFA-silica composite-derived carbon replica exhibits a highly faithful negative (inverse) structure of the SBA-15 porous framework [60]. With this in mind, we anticipated that the strategy of carbon replication may also bring an interesting insight into an alteration of textural and structural characteristics of SBA-15 along with an increasing degree of pseudomorphic transformation thereof. Previously, such approach has been successfully used for characterization of plugged SBA-15 [79].

Apparently, the inverse carbon replication may serve as a smart tool for investigation of the PT mechanism in a non-direct manner. To the best of our knowledge, herein we report on such concept for the first time. A thorough study on morphology, textural and structural characteristics of converted silicas and their carbon counterparts supported by TEM imaging and dynamic light scattering measurements led us to elucidate changes occurring in the silica porous structure at different degrees of PT. The results provide convincing evidence for the mechanism of *homogeneous transformation* of the pore structure of SBA-15 into MCM-41.

Experimental section

Synthesis of silica matrices and carbon replicas

All chemicals were commercially available and used without further purification: tetraethyl orthosilicate (TEOS, 98.0%, Acros Organics), poly(ethylene oxide)-*block*-poly(propylene oxide)-*block*-poly(ethylene oxide) amphiphilic triblock copolymer (Pluronic P123, Sigma-Aldrich), octyltrimethylammonium bromide (OTAB, ≥98.0%, Sigma-Aldrich), dodecyltrimethylammonium chloride (DTAC, 50% isopropanol/water 40/10 solution, Sigma-Aldrich), dodecyltrimethylammonium bromide (DTAB, ~99%, Sigma-Aldrich), hexadecyltrimethylammonium chloride (CTAC, 25% water solution, Sigma-Aldrich), hexadecyltrimethylammonium bromide (CTAB, ≥96.0%, Sigma-Aldrich), ammonia solution ($NH_{3\ aq}$, 25%, Avantor Performance Materials Poland), sodium hydroxide (NaOH, >98.0%, Avantor Performance Materials Poland), furfuryl alcohol (FA, 98%, Sigma-Aldrich), hydrochloric acid (HCl,

35%, Avantor Performance Materials Poland), hydrofluoric acid (HF, 40%, Avantor Performance Materials Poland), isopropanol (≥99.5%, Sigma-Aldrich), and 2-butanone (≥99.0%, Sigma-Aldrich).

SBA-15, MCM-41_C12 and MCM-41_C16

Mesoporous silica SBA-15 was synthesized under the acidic conditions at a molar gel composition as given in Table 1, according to the procedure reported elsewhere [59,77,78] after a twofold enlargement of the synthesis scale. The resulting material was labelled as SBA-15. The detailed synthesis procedure is described in Supporting information. Two reference MCM-41 materials with different pore sizes were synthesized under basic conditions using quaternary *N,N,N*-trimethyl*alkyl*ammonium chlorides as the SDA, where the *alkyl* fragments were *n-dodecyl* (DTAC (C12)) and *n-hexadecyl* chains (CTAC (C16)), respectively. The syntheses were carried out using the procedure described in the previous works [31,80] at the molar gel compositions shown in Table 1. The materials were denoted as MCM-41_C12, and MCM-41_C16, where the C12 and C16 suffixes correspond to the length of the *alkyl* fragments in the SDA used. Again, the details on the synthesis are given in Supporting information.

Pseudomorphic transformation of SBA-15

Pseudomorphic transformation of SBA-15 into MCM-41-like materials was carried out according to the procedure described by Reber and Brühwiler [70]. The syntheses were performed under basic conditions using quaternary *N,N,N*-trimethyl*alkyl*ammonium bromides as the SDA, where the *alkyl* fragments were *n-octyl* (OTAB (C8), *n-dodecyl* (DTAB (C12)) and *n-hexadecyl* chains (CTAB (C16)), respectively. The degree of pseudomorphic transformation was controlled by a silica/NaOH mass ratio (m_{silica}/m_{NaOH}; NaOH acts as a mother-silica dissolving agent), while a mass ratio of silica/surfactant (m_{silica}/m_{SDA}) was adjusted to achieve a constant molar ratio of $n_{silica}/n_{SDA} = 0.10$. Details on the pseudomorphic transformation procedure are gathered in Table 2.

Three equivalent portions of 13.39 g of sodium hydroxide solution (0.65 g of NaOH dissolved in 60.82 g of H_2O) were introduced into three 25 cm^3 polypropylene sealed vessels. Then, the proper amount of respective quaternary ammonium halides were added (i.e. 0.84 g of OTAB, 1.03 g of DTAB, and 1.21 g CTAB, respectively), and the mixtures were agitated vigorously until clear solutions were obtained. An amount of 2.00 g of freshly calcined SBA-15 was added to each vessel and the mixtures were shaken thoroughly for 5 min. Subsequently, the sealed vessels were transferred to an electric oven and kept statically under isothermal conditions at 100 °C for 6 h. Afterwards, the slurries were cooled down to room temperature, and the solid products were filtered, washed with distilled water and dried at room temperature overnight. Finally, the surfactants were removed by calcination of the materials in a muffle furnace at 550 °C for 12 h at a heating rate of 1 °C min^{-1}. The converted silicas were labelled as S_C8_14, S_C12_14, and S_C16_14, where C8, C12, and C16 represent OTAB, DTAB, and CTAB, respectively, and the suffix 14 - the m_{silica}/m_{NaOH} ratio.

Table 1
Molar gel compositions used in the syntheses of the starting silica materials.

Material	TEOS	SDA[a]	pH adjusting agent[b]	Co-solvent[c]	H_2O
SBA-15	1.00	0.02	2.94	–	116.46
MCM-41_C12	1.00	0.35	2.73	1.24	144.09
MCM-41_C16	1.00	0.16	2.73	–	151.53

[a] P123 for SBA-15, DTAC (C12), and CTAC (C16) for MCM-41_C12 and MCM-41_C16, respectively.
[b] HCl for SBA-15, and $NH_{3\ aq}$ for MCM-41 materials.
[c] Isopropanol (in the DTAC solution).

Table 2
Details on the procedure of pseudomorphic transformation of studied silicas.

Material	SDA	m_{silica}/m_{SDA}	m_{silica}/m_{NaOH}
S_C8_14	OTAB (C8)	2.38	14.00
S_C12_14	DTAB (C12)	1.95	14.00
S_C16_14	CTAB (C16)	1.65	14.00
S_C16_10	CTAB (C16)	1.65	10.00
S_C16_6	CTAB (C16)	1.65	6.00

Additionally, two materials based on the CTAB surfactant with higher degrees of pseudomorphic transformation were synthesized by proper adjusting the m_{silica}/m_{NaOH} ratio to higher alkalinity. In this case, the entire synthesis procedure, including the method of surfactant removal, was the same as for the S_C16_14 material, with only difference in the concentration of NaOH solutions. 13.39 g of solution containing 0.20 g or 0.33 g of NaOH was used, respectively, which correspond to m_{silica}/m_{NaOH} of 10 (S_C16_10) and 6 (S_C16_6), respectively.

Carbon replicas

The silicas upon PT were applied as the matrices for the preparation of a series of inverse carbon replicas. These materials were synthesized by the acid-catalyzed precipitation polycondensation of FA in an aqueous slurry of the silica matrix, following the procedure reported elsewhere [58–60,77,78]. The syntheses were carried out at the constant intended FA/silica mass ratio equal to 2.00, and the catalyst (HCl)/FA molar ratio of 4.00. An amount of 0.80 g of the freshly calcined silica matrix was added to a mixture containing 1.60 g of FA and 34.00 g of distilled water in a two-neck round-bottom flask (100 cm^3), placed in an oil bath and equipped with a reflux condenser, a magnetic stirrer and a small dropping funnel filled with 6.0 cm^3 of concentrated HCl. After stirring the mixture for 30 min at room temperature, HCl was instilled carefully (10 drops/min) and heating was turned on. After reaching 100 °C, the mixture was isothermally kept at this temperature for next 6 h under vigorous stirring (ca. 400 rpm). Afterwards, the resulting dark brown precipitate of PFA/silica composite was separated, washed with distilled water and dried at 90 °C overnight. Subsequently, the PFA/silica composites were carbonized in a tubular quartz furnace under an inert atmosphere (N_2, 40 cm^3 min^{-1}) at 850 °C for 4 h using a heating rate of 1 °C min^{-1}. Finally, the silica template was removed by double leaching with HF at room temperature for 90 min (each time 1.00 g of the carbonizate was immersed in 30.0 cm^3 of 5% HF solution). The ultimate replicas based on S_C8_14, S_C12_14, S_C16_14, S_C16_10, and S_C16_6 were marked as C_C8_14, C_C12_14, C_C16_14, C_C16_10, and C_C16_6, respectively. According to the foregoing procedure, two reference carbon materials, namely typical CMK-3 replica and C_MCM, were obtained by nanoreplication of pristine SBA-15 and MCM-41_C16 silicas, respectively.

Characterization

Textural parameters of the materials were examined by means of low-temperature adsorption–desorption of nitrogen (−195.8 °C) using a conventional volumetric technique. The isotherms were recorded on an ASAP 2020 instrument (Micromeritics). Prior to the measurements, the samples were outgassed at 250 °C for 6 h (silicas) or 4 h (carbon replicas). Specific surface areas (S_{BET}) were determined based on the multipoint Brunauer–Emmett–Teller model within the relative pressure (p/p_0) range of 0.05–0.20 [60,81,82]. Furthermore, external surface areas (S_{ext}) of the silica materials were computed based on slopes of linear functions fitted to standard reduced adsorption plots (α_s) in the ranges of

α_s = 1.25–1.90 and α_s = 1.65–2.25 for MCM-41 and SBA-15, respectively [60]. Excepting the typical CMK-3 material, calculations of S_{ext} for the carbon replicas were skipped due to curvature of adsorption branches of isotherms at $p/p_0 \rightarrow 1$ (lack of a *plateau*). The *t*-plot model (based on the de Boer equation) was employed for calculations of micropore surface within the p/p_0 range of 0.05–0.20. The α_s plots for the silica materials were calculated with respect to the reference macroporous silica LiChrospher Si-1000 [83], while for the carbon replicas the non-porous carbon reference LMA10 [84] was used. The micro- and mesopore volumes (V_{micro} and V_{meso}, respectively) of the pristine silicas were calculated based on y-intercepts of linear functions fitted to the α_s plots within the ranges of α_s = 0.30–0.90 and α_s = 1.25–1.90 for the MCM-41 materials and α_s = 0.60–1.25 and α_s = 1.65–2.25 for SBA-15, respectively [31,60]. In the case of the SBA-15 silicas after PT, the α_s range employed for the micropore volume calculations was constrained to α_s = 0.30–0.80 due to the presence of additional inflection on the isotherm caused by the formation of MCM-41-like porosity. Single-point total pore volumes (V_{total} s-p) were extracted from the isotherms using respective data points of adsorption branches at p/p_0 = 0.97–0.98 [31,60,85]. The mesopore volumes of carbon replicas (V_{meso}) were calculated by subtracting the micropore volume (α_s model) from the single-point total pore volumes. The same approach was employed to assess the V_{meso} values of the transformed silica materials exhibiting the lack of a *plateau* in the $p/p_0 \rightarrow 1$ region of the adsorption isotherm (i.e. S_C8_14, S_C12_14, and S_C16_14).

The non-local density functional theory Kernel (NLDFT; adsorption branch of isotherm; cylindrical pore symmetry assumption) was applied to compute the pore size distribution curves (PSDs) of the silicas ($D_{pore,DFT}$), whereas the quenched solid density functional theory model (QSDFT; equilibrium model; slit-like pore geometry; software ASIQwin^{TM} ver. 1.11, Quantachrome Instruments) and the 2D-NLDFT model for carbons with heterogeneous surfaces (SAIEUS Program, ver. 3.0 by Jacek Jagiello) were used for calculation of the PSDs of the carbon replicas [81,82,85–89].

The foregoing DFT models were also used for the simulation of the DFT nitrogen isotherms based on the measured adsorption branches data. The fitting enabled us to compare directly the behavior of the isotherms of the relevant modified materials with those mother ones by plotting the nitrogen uptakes of a particular sample (measured at given p/p_0 values) vs. the reference material (i.e. pristine SBA-15 and MCM-41 for silicas, and CMK-3 for carbon replicas). The fitting errors did not exceed 1.00%.

The average wall thicknesses for pristine silicas, their relatives after PT and carbon replicas were estimated based on textural and structural parameters according to the approaches reported by others [90,91]. The details on these calculations are presented in Supporting information.

Structural parameters of the studied materials were determined by means of low-angle X-ray powder diffraction (XRD) using a Bruker D2 Phaser instrument equipped with a LYNXEYE detector. The XRD patterns were recorded with Cu Kα

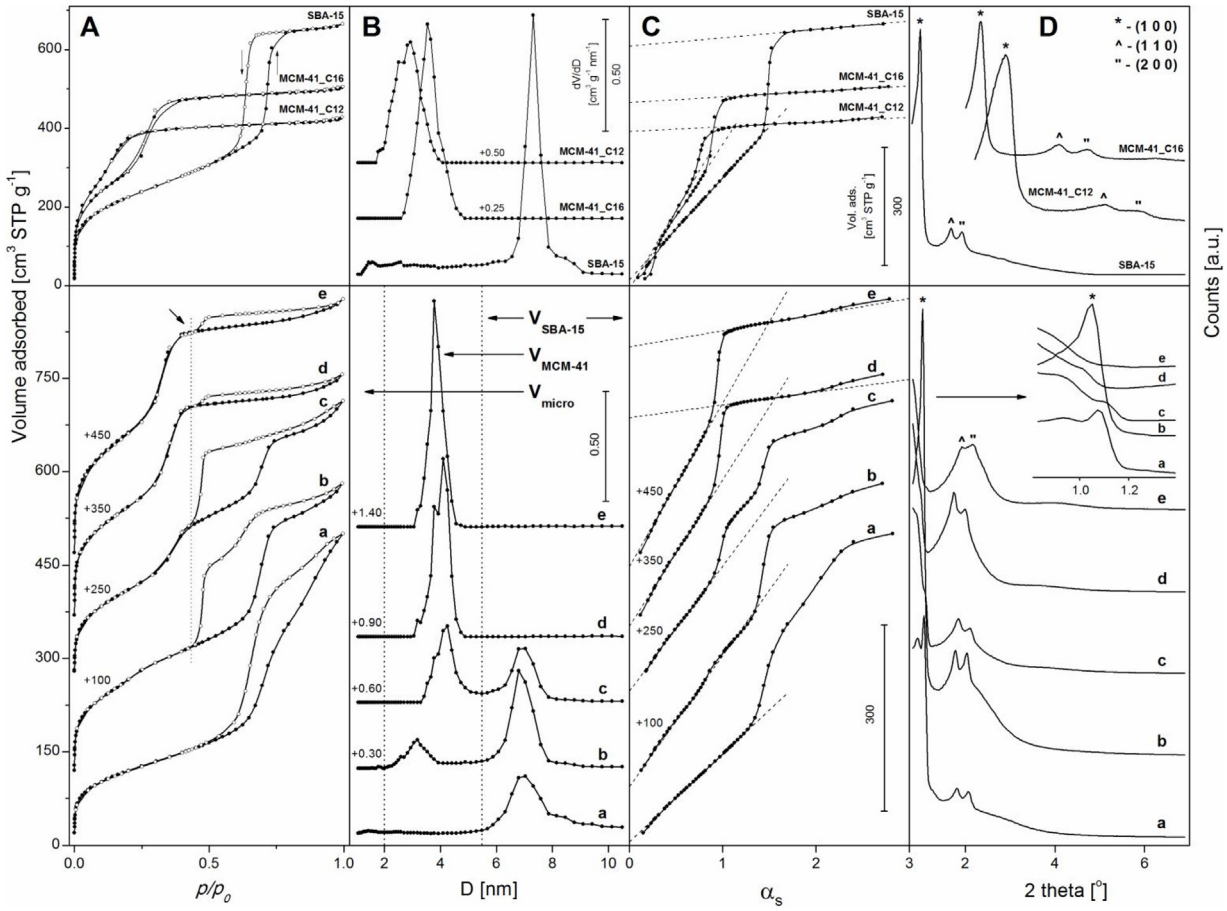

Fig. 1. N_2 adsorption–desorption isotherms (filled and open symbols, respectively; the characteristic closure points at p/p_0 = 0.43 marked by arrow and dotted line) (A), respective PSDs (NLDFT) (B), α_s plots (C), and low-angle XRD patterns (D) collected for pristine silicas (top), and S_C8_14 (a), S_C12_14 (b), S_C16_14 (c), S_C16_10 (d), and S_C16_6 (e) (bottom).

radiation (λ = 1.54184 Å) in a 2θ range of 0.75–7.00° with a step of 0.02°. Due to the featureless XRD diffractograms in the (1 0 0) reflection region, the d_{100} interplanar spacing for the silicas after PT was calculated based on the angular position of the adjacent (2 0 0) plane as $d_{100} = 2 \cdot d_{200}$ [9,91].

Transmission electron microscopy (TEM) imaging was performed on an FEI Tecnai TF20 X-TWIN (FEG) microscope working at an accelerating voltage of 200 kV. Prior to the analyses, the samples (dispersed in isopropanol and sonicated for 10 min) were deposited onto carbon-coated copper TEM grids by drop casting.

Thermogravimetric measurements (TG) were carried out using a SDT Q600 analyzer (TA Instruments). An amount of ca. 0.01 g of a sample placed in a corundum crucible was heated from 30 to 1000 °C at a heating rate of 20 °C min^{-1} at flowing air (100 cm^3 min^{-1}). The real PFA/silica mass ratios in the as-synthesized composites were determined based on the mass loss recorded during the TG measurement, while the pore filling degree was calculated as the ratio of bulky PFA volume (density of bulky polymer was assumed to be 1.55 g cm^{-3} [60]) with respect to the single-point total pore volume of the relevant silica matrix.

Volumetric particle size distributions were determined from dynamic light scattering measurements (DLS) undertaken using a Zetasizer Nano ZS analyzer (Malvern Instruments) working at 25 °C. Prior to the measurements, a suspension containing 0.1 wt.% of a material was prepared using distilled water (silicas) or 2-butanone (carbons), and sonicated in an ultrasonic bath for 15 min.

Results and discussion

Structural and textural characteristics of the silicas

Textural and structural features of the parent SBA-15 and MCM-41 silicas, as well as the SBA-15 analogues after PT were studied by low-temperature adsorption–desorption of nitrogen and low-angle X-ray diffraction. The recorded isotherms, relevant PSDs, α_s plots, and XRD patterns are depicted in Fig. 1, while the corresponding textural and structural parameters are compiled in Table 3.

The isotherm for parent SBA-15 is a textbook example of the type IV(a) according to the updated IUPAC conventional classification [81] with a well-pronounced distinctive H1 hysteresis loop within the relative pressure range of p/p_0 = 0.60–0.80 ascribed to the delayed capillary condensation of adsorptive in mesochannels [31,60,81,82,85]. The presence of the hysteresis loop arises from the variation of diameter along the mesopores (i.e. corrugations of the interior walls). The narrow PSD profile (cf. Fig. 1B) evidences the presence of primary mesopores uniform in diameter of 7.3 nm accompanied by the minor share of small mesopores (2.0–4.0 nm, centered at ca. 2.6 nm) and the small fraction of micropores with the pore size of 1.4 nm. These narrower pores play the role of the interconnecting channels between the parallelly-oriented main mesopores and form around them so-called *micropore corona* [31,60,85,89]. The adjacent primary mesochannels are separated from each other by the walls of a thickness of 3.0 nm. The mixed micro-mesoporous character of the material is evident when considering the α_s plot (cf. Fig. 1C). The total pore volume equals 1.02 cm^3 g^{-1} with about 2% contribution of micropores (0.02 cm^3 g^{-1}; cf. Table 3). Naturally, this microporosity is also reflected in the specific micropore surface of 25 m^2 g^{-1}. The BET surface of SBA-15 is 815 m^2 g^{-1} with the external surface of 62 m^2 g^{-1}. Such textural parameters are in line with the respective values reported in the literature [9,14–16,19,20,30,31,33].

In the case of MCM-41_C16 the nitrogen isotherm is of IV(a) type with a vastly narrow H1 hysteresis loop, while that one for MCM-41_C12 is clearly reversible (IV(b) type) [31,32,80–82,85]. This is due to the prominently smaller pores of the MCM-41 materials compared to SBA-15. The rapid increase in the nitrogen uptake related to capillary condensation is visible within the p/p_0 range of 0.10–0.30 and 0.20–0.40 for MCM-41_C12 and MCM-41_C16, respectively, and arises from the presence of mesopores of diameters of ca. 2.9 and 3.5 nm, respectively (NLDFT model). The respective total pore volumes are equal to 0.65 and 0.78 cm^3 g^{-1}. Both MCM-41 materials exhibit the wall thickness of 0.7 nm, being therefore substantially thinner compared to SBA-15 (more than fourfold). This is typical of the M41S family materials [17,18,21,22,28,29,31,32,34,80]. In contrast to SBA-15, the analysis of the α_s plots for the MCM-41 silicas points to a purely

Table 3
Textural and structural parameters of parent SBA-15 and MCM-41, SBA-15 after pseudomorphic transformation and corresponding carbon replicas.

Sample	S_{BET} (S_{ext}[a]) [m^2 g^{-1}]	S_{micro} [m^2 g^{-1}] *t*-plot	V_{total} [cm^3 g^{-1}] s-p	V_{micro} [cm^3 g^{-1}] α_s	V_{meso} [cm^3 g^{-1}]	D_{pore} [nm]	D_{wall} [nm]	a_0 [nm]
SBA-15	815 (62)	25	1.02	0.02	0.92[a], 1.00[b]	1.4, 2.6, 7.3[d]	3.0[f]	10.3[h]
MCM-41_C12	1529 (35)	0	0.65	0.00	0.61[a], 0.65[b]	2.9[d] (2.8)[c]	0.7[e]	3.5[h]
MCM-41_C16	1063 (41)	0	0.78	0.00	0.72[a], 0.78[b]	3.5[d] (3.6)[c]	0.7[e]	4.3[h]
S_C8_14	435	13	0.75	0.01	0.74[b]	1.4, 7.3[d]	2.6[f]	9.9[i]
S_C12_14	606	0	0.72	0.00	0.72[b]	3.2, 6.8[d]	6.8, 3.2[f]	10.0[i]
S_C16_14	585	0	0.70	0.00	0.70[b]	4.3, 6.8[d]	5.2, 2.7[f]	9.5[i]
S_C16_10	708 (60)	0	0.61	0.00	0.52[a], 0.61[b]	4.1[d]	6.2[f]	10.3[i]
S_C16_6	783 (76)	0	0.65	0.00	0.54[a], 0.65[b]	3.8[d]	5.6[f]	9.4[i]
C_C8_14	1117	188	1.13	0.12	1.01[b]	1.2, 3.4[d]	7.2[g]	11.2[h]
C_C12_14	1175	107	1.11	0.08	1.03[b]	1.1, 3.4[d]	7.0[g]	11.2[h]
C_C16_14	1122	107	1.06	0.08	0.98[b]	1.1, 3.4[d]	7.1[g]	11.2[h]
C_C16_10	1041 (129)	252	0.76	0.15	0.61[b]	1.0, 3.4[d]	–	–[j]
C_C16_6	1068 (124)	173	0.78	0.12	0.66[b]	1.0, 3.4[d]	–	–[j]
CMK-3	1115 (36)	105	0.92	0.08	0.84[b]	1.1, 3.1[d]	6.1[g]	9.2[h]
C_MCM	781 (38)	335	0.46	0.18	0.28[b]	0.9, 3.4[d]	–	–[j]

[a] α_s model.
[b] $V_{meso} = V_{total\ (s-p)} - V_{micro\ (\alpha s)}$.
[c] $D_{pore,K-J-S}$ (Eq. (S1)).
[d] $D_{pore,DFT}$.
[e] $D_{wall,K-J-S}$ (Eq. (S2)).
[f] $D_{wall,DFT}$ (Eq. (S3)).
[g] Calculated from Eq. (S5).
[h] Calculated from (1 0 0) reflection.
[i] Calculated from (2 0 0) reflection as $d_{1\,0\,0} = 2 \cdot d_{2\,0\,0}$.
[j] Featureless XRD diffractogram (Fig. 4).

mesoporous character thereof (cf. Fig. 1C; Table 3), which is also consistent with the former reports [31,41,46]. Obviously, the narrow pores and thin walls of both MCM-41 materials result in significantly higher specific surface areas than that of SBA-15 (i.e. 1529 and 1063 $m^2 g^{-1}$, with the external surfaces of 35 and 41 $m^2 g^{-1}$ for MCM-41_C12, and MCM-41_C16, respectively).

The low-angle XRD patterns for the pristine SBA-15 and MCM-41 materials (Fig. 1D) show three well-distinguished Bragg's diffraction reflections indexed as (1 0 0), (1 1 0), and (2 0 0), typical of a long-range 2D ordering of hexagonal symmetry of mesostructure classified as the p6mm space group [5,9,14–17,31,32,60]. The (1 0 0) reflections for MCM-41_C12, MCM-41_C16, and SBA-15 centered at 2.89, 2.35, and 0.99° 2θ, respectively, correspond to the a_0 lattice parameters of 3.5, 4.3, and 10.3 nm (cf. Table 3). These values turn out to be reliable when combined with the corresponding pore diameters.

The changes in the textural and structural characteristics of the SBA-15 material after PT into the MCM-41-like mesostructure were investigated in terms of: (i) an influence of length of *alkyl* chain in a surfactant utilized for pseudomorphic transformation (i.e. C8, C12, and C16), and (ii) an effect of SBA-15 conversion degree for a chosen surfactant *alkyl* chain length (i.e. C16), on the features of the ultimate silica. The relevant nitrogen adsorption isotherms are displayed together with the respective PSDs, α_s plots and XRD patterns in the bottom part of Fig. 1, while the corresponding textural parameters are summarized in Table 3. Undoubtedly, regardless of the type of the used SDA as well as the alkalinity of the reaction mixture, the PT of SBA-15 resulted in a considerable alteration of the shape of nitrogen adsorption isotherms.

The isotherm recorded for the S_C8_14 material (IV(a) type with H2(b) hysteresis loop) [70,74,75,81,82,85] (Fig. 1A–a) indicates a partial collapse of the mother SBA-15 framework. This type of hysteresis is assigned to pore blocking in solids with broad cages (viz. voids created by leaching of silica) interconnected by relatively large necks (intact primary mesopores of SBA-15). This is clearly reflected in the pore size distribution profile (Fig. 1B). The intensity of the maximum of PSD is considerably lower, while its width is significantly broadened towards larger size compared to the pristine SBA-15. In fact, the strongly basic reaction medium caused the partial dissolution of silica, but the expected new fraction of smaller mesopores originating from the incorporation of the OTAB micelles into the silica walls has not been emerged. This is clearly supported by the textural parameters, i.e. considerable decline in the specific surface area (close to twofold lower than starting SBA-15) as well as a twofold decrease in the micropore volume and surface (cf. Table 3). Besides, the deterioration of the structure is manifested by a drop of the total pore volume (mainly in the mesopore range) by ca. 26%. Furthermore, the leaching of the silica is accompanied by a disappearance of the narrower interconnecting mesopores (2.0–4.0 nm), as well as the diminished average wall thickness.

In contrast, a deeper alteration of the shape of isotherm was observed in the case of the SBA-15 upon PT of a moderate degree with the use of DTAB and CTAB surfactants (Fig. 1A–b, c). These isotherms exhibit a IV(a) type with well-distinguished H2(a) hysteresis loops featuring the three pronounced steps in the desorption branch and the constant closure points at $p/p_0 = 0.43$ notwithstanding the real diameter of the pore neck. Such behavior of hysteresis is distinctive of bimodal mesoporous materials possessing cage-like pore structures. As a consequence, the liberation of these confined spaces is governed by the mechanism of cavitation-induced evacuation [31,70,81,82,85]. The further increase in the PT degree (Fig. 1A–d, e) implies an alteration of the shape of the isotherms towards IV(b) (typical of MCM-41) with distinguished H4 hysteresis loops [81,85].

Expectedly, for the materials of a moderate degree of PT (i.e. S_C12_14 and S_C16_14, Fig. 1B) the mixed bimodal porosity is observed. The larger pores originate from the pristine SBA-15 material, while the size of the smaller channels is governed by the length of the *alkyl* chain in the respective SDA utilized. Theoretically, the PSDs of these silicas should reveal the pore size exact as respective typical MCM-41 references thereof (cf. Fig. 1B). However, as seen, both MCM-41 silicas exhibit slightly lower mesopore sizes (i.e. 2.9 and 3.5 nm for MCM-41_C12 and MCM-41_C16, respectively, vs. 3.2 and 4.3 nm for S_C12_14 and S_C16_14, respectively, see Table 3 and Fig. 1B). These discrepancies arise from the disparities in the synthesis conditions (i.e. alkalinity, type of silica source, different surrounding of the surfactant's micelles in the confined spaces of the SBA-15 mesopores in the case of PT, compared to the synthesis of MCM-41 *de novo* in an aqueous medium) [70].

More interestingly, the pore size of the MCM-41-like fraction is clearly influenced by the degree of SBA-15 transformation. Namely, the degree of transformation is higher, the PSDs of the newly-formed mesopores are closer to that typical of MCM-41 (Table 3, S_C16_14, S_C16_10, and S_C16_6 with PSDs centered at 4.3, 4.1, and 3.8 nm, respectively).

Obviously, the higher degree of transformation entails also a gradual drop in the pore volume contributed by the original porosity of SBA-15. Interestingly, the PSDs of the partially transformed samples (i.e. S_C12_14, and S_C16_14, Table 3) reveal a subtle shift (by ca. 0.5 nm) towards smaller mean pore size compared to those of the parent SBA-15. This effect is most likely due to the repeated calcination of the materials after PT.

The shares of the particular pore volumes in V_{total} for the respective silicas upon PT are presented in Fig. 2 (the corresponding pore size ranges are distinguished in Fig. 1B). It is pertinent to mention that the PT process carried out under the same conditions (i.e. m_{silica}/m_{SDA} ratio, equivalent pH) but applying different SDAs does not provide the formation of the silicas of a comparable transformation degree. Nevertheless, notwithstanding the type of the SDA used, PT entails a remarkable decline in the micropore volume and micropore surface (Table 3, S_C8_14) or, in a boundary case, even its disappearance (S_C12_14 and all S_C16). Similar observations were also reported by others [70]. A plausible explanation of the extinction of microporosity may be the effect of fusing (coalescence) of the adjacent micropores caused by leaching of silica due to high pH. Furthermore, PT results in a decrease in the total pore volume (mainly mesopores, cf. Table 3), which in turn implies a noticeable reduction of the specific surface area. In this regard, an interesting insight is provided by the analysis of wall

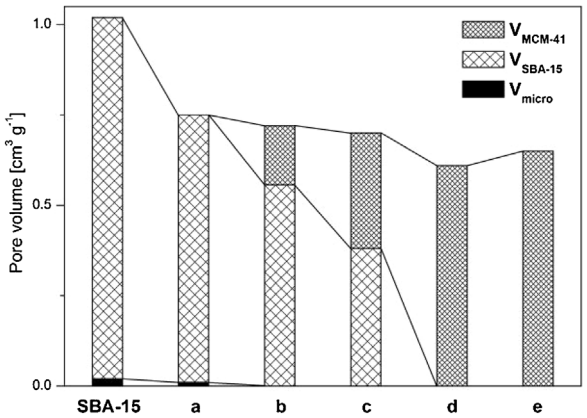

Fig. 2. Contributions of the particular pore volumes to V_{total} of the pristine SBA-15, S_C8_14 (a), S_C12_14 (b), S_C16_14 (c), S_C16_10 (d), and S_C16_6 (e) (the lines connecting the columns added to guide the eyes).

thickness for the S_C12_14 material and all the S_C16 silicas (Table 3). It can be inferred that during PT the walls of the pristine SBA-15 (with thickness of 3.0 nm) are gradually replaced by thicker walls (of ca. 5.2–6.8 nm), whereas the value of the a_0 lattice parameter does not vary prominently. Interestingly enough, this suggests that each single primary mesopore of pristine SBA-15 is transmuted into one narrower MCM-41-like channel (see Fig. 6B inset).

Eventually, along with the progress of the transformation, the original SBA-15 porosity disappears, and MCM-41-like structure with thick walls (i.e. 5.6 nm, thereby eightfold thicker than for typical MCM-41), none microporosity, a relatively low surface area (783 $m^2 g^{-1}$), and a moderate total pore volume (0.65 $cm^3 g^{-1}$) is formed (Table 3, S_C16_6). Indeed, such textural parameters are reasonable considering the thickening of the silica walls upon PT. The MCM-41-like character of this material is additionally proven by the shape of the nitrogen isotherm (Fig. 1A–e). As mentioned, the narrow hysteresis loop within p/p_0 = 0.43–1.00 indicates the presence of intrinsic *bottleneck* cavities being perhaps an artifact inherited from the SBA-15 structure. This effect was also noticed by other researchers and it seems to be an inherent feature of the silicas prepared by PT [70,74].

A closer inspection of the behavior of the isotherms recorded for the materials after PT with regard to the pristine references (i.e. SBA-15 and MCM-41) was feasible through the simulation of NLDFT isotherms, which were fitted to the collected adsorption branches. The computed dataset for the PT-silicas was then plotted vs. the respective parent silicas. The relevant plots are depicted in Fig. S1 (Supporting information). The lower slopes of the nitrogen adsorption isotherms in the range of the nitrogen uptake of 0–250 $cm^3 g^{-1}$ for the PT-silicas vs. SBA-15 and MCM-41 (Fig. S1A and B, respectively) clearly confirm the lower surface areas of these materials compared to both reference silicas (Table 3), however, their linear character exhibits the mutual similarity thereof. The increasing degree of transformation results in an increasingly distinguished characteristic *knee* within the range of nitrogen uptake of 250–450 $cm^3 g^{-1}$ (Fig. S1A), which reveals their gradually increasing similarity to MCM-41. As expected, the highest degree of similarity to MCM-41_C16 was found for the S_C16_6 material (Fig. S1B).

Carbon nanoreplication: polymerization efficiency

The efficiency of deposition of PFA in the pore systems of the silicas was determined by thermogravimetric measurements in an oxidizing atmosphere (PFA underwent the total oxidation into volatiles, while a mass of residual silica allowed us calculating real content of the organic part). The polymer/silica mass ratios together with the pore filling degrees are presented in Fig. 3.

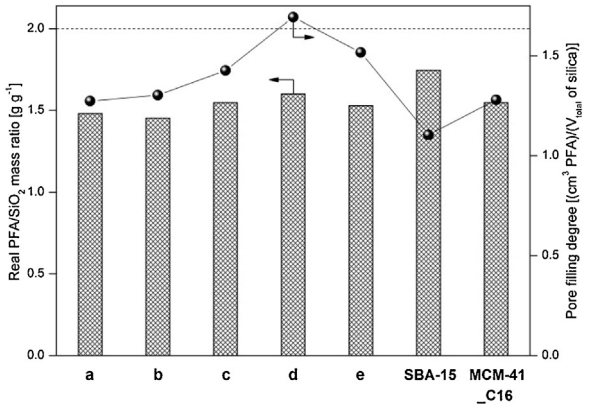

Fig. 3. Effectiveness of PFA deposition in the pore systems of the silica matrices: S_C8_14 (a), S_C12_14 (b), S_C16_14 (c), S_C16_10 (d), S_C16_6 (e), SBA-15 and MCM-41_C16 (the dashed line represents the intended PFA/SiO_2 mass ratio; the lines merging the dots added to guide the eyes).

The lower polymer contents compared to the intended mass ratio of 2.00 arise from the loss of a portion of FA in the form of water-soluble oligomers separated from the materials after the synthesis of the PFA/silica composites [32,34,59,60,77,78]. The highest effectiveness of PFA accumulation (i.e. 87.3%) was achieved for SBA-15, however, the respective pore filling degree (110.4%) is the lowest one among the studied mesoporous silicas. Although the efficiency of PFA deposition onto the pseudomorphically transformed silicas and MCM-41_C16 is slightly lower, varying between 72.7% and 80.0% for S_C12_14 and S_C16_10, respectively, the pore filling degrees are noticeably higher than for SBA-15 (i.e. 127.4% and 169.3% for S_C8_14 and S_C16_10, respectively). This is due to the lower total pore volumes of the transformed silicas compared to the pristine SBA-15 (cf. Table 3). Nonetheless, the pore filling degrees exceeding 100% suggest that in all cases the pore systems of matrices underwent the complete filling with the carbon precursor, and the excessive polymer covers the external surface of the silica particles as reported elsewhere [60,77,78].

Structural and textural characteristics of carbon replicas

The structural and textural parameters of the ultimate carbon replicas were investigated by low-angle X-ray powder diffraction and low-temperature adsorption–desorption of nitrogen. The collected results are presented in Fig. 4.

The isotherm recorded for the true CMK-3 replica is characteristic of IV(a) type according to the IUPAC classification with a H2(a) hysteresis loop (the desorption branch within p/p_0 = 0.35–0.45 is prominently steeper than the adsorption one) [81,82,85,86]. The relatively high nitrogen uptake at the lowest relative pressures (close to 200 cm^3 STP g^{-1}) and the distinguished inflection at $p/p_0 \approx$ 0.01–0.10 point to the presence of an abundant share of micropores (cf. Table 3). The pronounced step of capillary condensation at p/p_0 = 0.40–0.60 together with a narrow hysteresis loop indicate the presence of mesopores uniform in size. The PSD calculated according to the QSDFT model reveals a mixed micro-mesoporous character with the micropore size of 1.1 nm and the main mesopore diameter of 3.1 nm (Fig. 4B; Table 3). The specific surface area of 1115 $m^2 g^{-1}$ with ca. 9.5% contribution of micropore area and the total pore volume of 0.92 $cm^3 g^{-1}$ with the micropore fraction of 0.08 $cm^3 g^{-1}$ are coherent with the typical parameters of CMK-3 [59,60,77,78]. The wall thickness (or, alternatively, the average diameter of the carbon rods in the case of carbon replicas) of 6.1 nm seems to be reliable, considering that the mesopores of the parent SBA-15 (of 7.3 nm diameter) undergo shrinkage during carbonization. It is pertinent to mention that the external surface area of a few dozen $m^2 g^{-1}$ suggests that the replica most likely retains the morphology of grains of the mother silica matrix. The XRD pattern collected for the CMK-3 replica resembling the corresponding diffractogram for the pristine SBA-15 (Figs. 1D and 4C, respectively) clearly proves the preservation of the structural array of the silica matrix. Therefore, although the CMK-3 material exhibits the inverse structure of SBA-15, it is also classified as the p6mm space group [58–60,62,77,78].

The alteration of the structural and textural features of the silicas after PT found reflection in the structures of the corresponding carbon replicas. The replicas derived from the silicas after PT using different SDAs but at the same alkalinity (i.e. the carbon homologues of the S_C8_14, S_C12_14, and S_C16_14 silicas, respectively; Fig. 4A–a-c) exhibit the nitrogen isotherms of the IV(a) type with relatively broad hysteresis loops of H2(b) shape, resembling rather the isotherm of the S_C8_14 sample than CMK-3 (cf. Figs. 1A–a and 4A, respectively) [31,60,81,82,85,86]. Such type

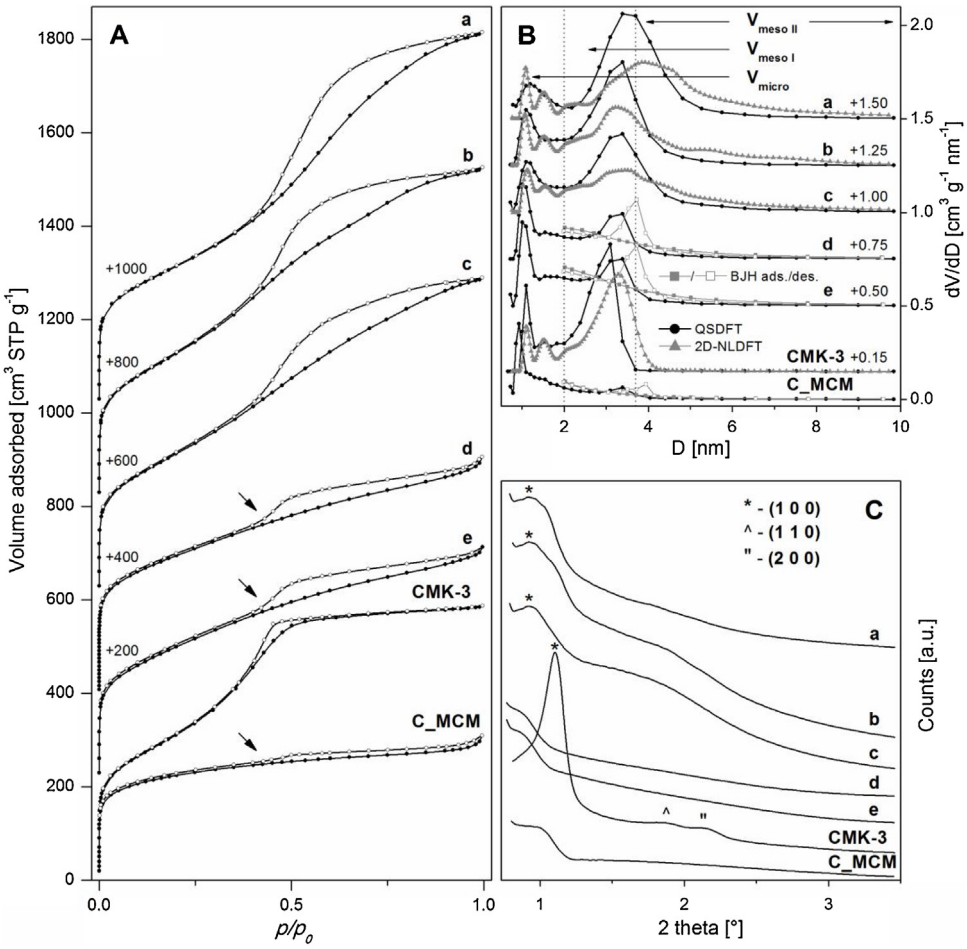

Fig. 4. N_2 adsorption–desorption isotherms (filled and open symbols, respectively; the characteristic closure points at $p/p_0 = 0.43$ marked by arrows) (A), respective PSDs (B), and low-angle X-ray powder diffraction patterns (C) for C_C8_14 (a), C_C12_14 (b), C_C16_14 (c), C_C16_10 (d), C_C16_6 (e), CMK-3 and C_MCM.

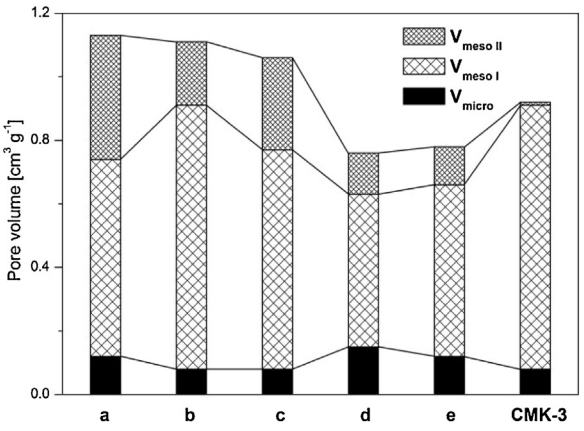

Fig. 5. Contributions of the particular pore volumes to the V_{total} in the studied carbon replicas – C_C8_14 (a), C_C12_14 (b), C_C16_14 (c), C_C16_10 (d), C_C16_6 (e), and CMK-3 (the lines connecting the columns added to guide the eyes).

of hysteresis is typical of materials with large pores constricted by smaller necks (but also relatively broad). Apparently, the partial leaching of the silica walls followed by the development of the MCM-41-like porosity inside the confined pore system of SBA-15 during PT results in the formation of cavities and smaller interconnecting necks to be subsequently filled with the carbon precursor. As a consequence, the ultimate replicas are constituted of carbon rods severely inhomogeneous in diameter along their length (i.e. resembling deeply corrugated carbon sticks). Thus, the final carbon framework features larger cages interconnected by smaller voids. Indeed, considering the substantially broader QSDFT PSDs for the discussed materials (additionally shifted towards larger sizes than CMK-3) (Fig. 4B), the presence of these much larger cavities in the interstitial space between the adjacent carbon rods is evident. This is well-pronounced in the shape of 2D-NLDFT curves, which clearly reveal bimodal mesoporosity for the replicas obtained from silicas after partial PT (namely, broader mesopores of ca. 5.5 and 4.5 nm for C_C12_14 and C_C16_14, respectively). Except the prominently higher total pore volume arising from the presence of these broader pores, other textural parameters of the replicas are in line with those of the true CMK-3 replica (cf. Table 3). Besides, a slightly broader average diameter of the carbon nanorods is due to the higher a_0 lattice parameters noticed. However, taking into account the relatively poor intensities of the (1 0 0) reflections for these materials (cf. Fig. 4C), care must be taken when considering the exactness of the angular positions of their maxima.

The analysis of the textural parameters of the replicas synthesized based on the silicas prepared using CTAB as SDA at varying alkalinity (namely the C_C16_14, C_C16_10, and C_C16_6 materials) brings certain interesting insights. As mentioned, the C_C16_14 material exhibits the nitrogen isotherm of the IV(a) type with H2(b) hysteresis loop, while in the case of the replicas obtained from the SBA-15 of higher degrees of PT (C_C16_10 and C_C16_6) the character of the isotherm alternates into the type I(b) commonly observed for micro-mesoporous materials possessing a

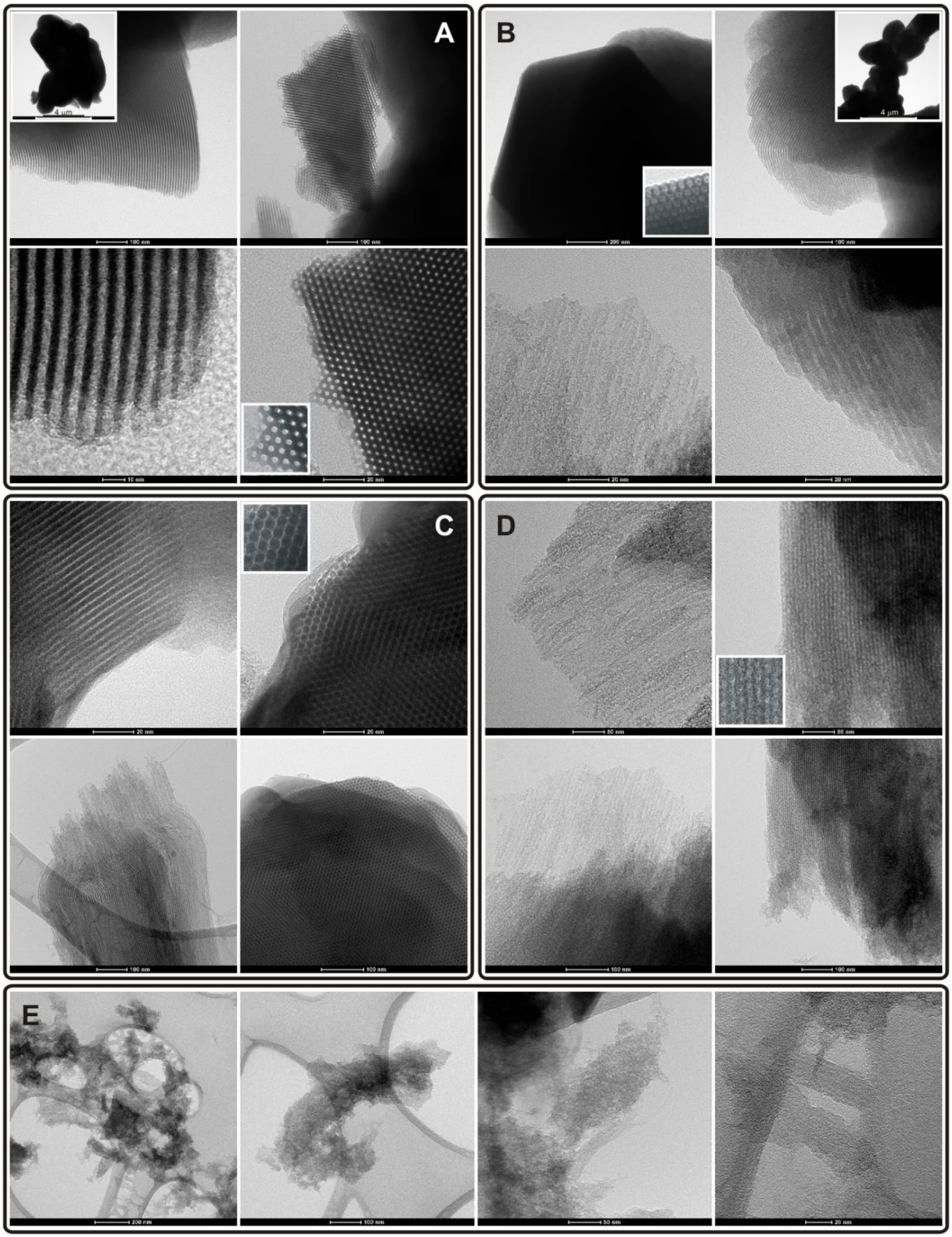

Fig. 6. TEM images of pristine SBA-15 (A), S_C16_14 (B), CMK-3 (C), C_C16_14 (D), and C_C16_6 (E).

minor share of narrow mesopores [81,85,86]. Interestingly enough, these isotherms exhibit pronounced H4 hysteresis loops with a distinguished step-down of the desorption branch at $p/p_0 = 0.43$ resembling those ones noticed for the corresponding starting silicas (Figs. 1A–d, e, and 4A–d, e; Table 3).

The isotherms shape confirms a gradual extinction of mesoporosity along with increase in degree of PT of the used silica matrix. Indeed, although the BET surface areas of all these materials remain at a constant level of ca. 1100 $m^2 g^{-1}$, a significant drop in the total pore volume is observed due to diminution in the

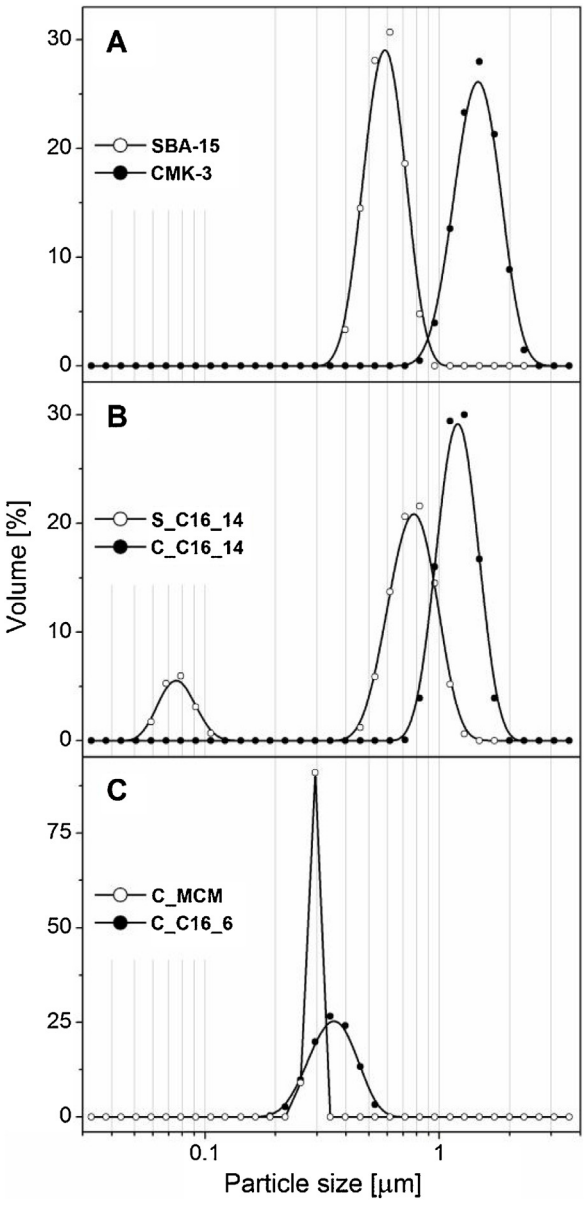

Fig. 7. Volumetric particle size distributions for parent SBA-15 and its carbon analogue CMK-3 (A), SBA-15 upon partial PT (S_C16_14) with respective carbon replica (C_C16_14) (B), and replica C_C16_6 cast from SBA-15 upon total PT (for sake of comparison, the profile for C_MCM replica originated from MCM-41_C16 was added) (C).

mesopore volume share. This is in line with the PSDs (cf. Fig. 4B). It is worth to note that although the QSDFT profiles for C_C16_10 and C_C16_6 show the maxima at 3.4 nm, the BJH PSDs calculated on the adsorption branches are clearly featureless in this region (Fig. 4B–d, e) (obviously, the relevant BJH profiles computed from desorption data points feature conspicuous artificial peaks at 3.7 nm). Therefore, the reliability of the QSDFT model in these particular cases is questionable. Consequently, the vestigial mesoporosity of these materials should be attributed rather to a minor fraction of the residual material, which has resisted the disintegration within the grain. Incidentally, this finding clearly shows that care must be taken when analyzing the PSDs for each particular material' series when based solely on a single calculation model.

The above considerations find reflection in the corresponding XRD patterns (Fig. 4C). The typical CMK-3 replica shows three well resolved reflections at the angular positions of 1.11°, 1.86° and 2.12°, attributed to the (1 0 0), (1 1 0), and (2 0 0) Miller indices, respectively, and assigned to the p6mm space group. The respective d_{100} interplanar spacing of 7.9 nm corresponds to the a_0 lattice parameter of 9.2 nm and carbon rods diameter equal to 6.1 nm, being in line with previously reported for suchlike materials (Table 3) [58–60,64,77,78]. On the other hand, the carbons derived from the partially transformed SBA-15 (i.e. C_C8_14, C_C12_14, and C_C16_14; Fig. 4C–a–c) exhibit a broad (1 0 0) reflection of a poor intensity centered at 0.92° corresponding to the d_{100} interplanar spacing of 9.7 nm and the a_0 lattice parameter of 11.2 nm, while the further two reflections partially overlap. This suggests that the use of the PT-silicas as matrices for nanocasting results in the formation of the materials being somewhat lower ordered than typical SBA-15, which is not surprising in view of the foregoing discussion. Furthermore, in the case of the replicas originating from the silicas of the utmost PT degrees (i.e. C_C16_10 and C_C16_6; Fig. 4C–d,e), the XRD patterns are almost featureless suggesting *ipso facto* nearly total collapse of the 3D framework (i.e. the disintegration that yields, let say, *rubble* of the separate carbon nanorods). This is in excellent compliance with the results of nitrogen sorption.

It is interesting to juxtapose the characteristics of the replicas synthesized from the matrices of the highest degrees of PT with the relevant data for the reference C_MCM. This counterpart sample exhibits the nitrogen isotherm similar to that of C_C16_10 and C_C16_6 (I(b) type with H4 hysteresis; Fig. 4A and Table 3), except a higher share of micropore volume and a lower contribution of mesopore volume. The latter effect is understandable in view of the lack of the interconnecting channels in the pristine MCM-41 resulting in the disintegration of the carbon structure after leaching of the silica scaffolding. A plausible explanation of the presence of narrow hysteresis loop in the isotherm of C_MCM may be a polymer shell formed around the silica particle during polycondensation of PFA. Such envelope could serve as a shield merging certain fragments of the carbon nanorods formed nearby the pore mouths of MCM-41. As a result, the material features a small contribution of mesopore volume (Table 3). The PSD reveals the dominant microporous nature of this material (Fig. 4B), while its featureless XRD pattern (Fig. 4C) conclusively evidences the profound collapse of the structure.

The shares of the particular pore volumes in V_{total} of the respective carbon replicas are gathered in Fig. 5 (the relevant pore size ranges are outlined in Fig. 4B).

The highest share of secondary mesoporosity ($V_{meso\ II}$) of ca. 39% in the overall mesoporosity ($V_{meso\ I} + V_{meso\ II}$) is observed in the case of the carbon material based on the S_S8_14 matrix (i.e. C_C8_14). This is understandable taking into account the poor quality of the structure of this silica caused by PT (cf. Section "Structural and textural characteristics of the silicas"). Interestingly, the contribution of $V_{meso\ II}$ decreases gradually for the carbons derived from the silicas synthesized with the CTAB surfactant with an increasing degree of PT. Namely, the shares of 30, 21 and 18% of $V_{meso\ II}$ with regard to the total mesopore volume were noticed for the C_C16_14, C_C16_10 and C_C16_6 replicas, respectively. Again, this clearly evidences the disintegration of the structures of the replicas originating from the silicas with the utmost PT degrees.

Considering the comparative QSDFT-fitted nitrogen adsorption isotherms of the studied replicas and typical CMK-3 material (Fig. S2) one may infer that all these materials exhibit mutual similarity in the micropore region (i.e. the nitrogen uptake up to 150 cm^3 STP g^{-1}). Moreover, except for the C_MCM, this similarity is maintained up to ca. 300 cm^3 STP g^{-1}, which reflects the comparable BET surface areas. Combining the lower adsorptive uptakes at the moderate relative pressures and prominently higher

nitrogen uptakes for the C_C8_14, C_C12_14 and C_C16_14 materials at $p/p_0 \rightarrow 1$ (cf. Fig. S2–a-c), the formation of the secondary mesopores at the expense of the partial extinction of the typical CMK-3-like porosity is evident. Finally, the highest similarity of the carbons originated from the silicas with the highest degrees of PT (cf. Fig. S2–d, e) with the character of the C_MCM material is obvious.

The morphology and structural ordering of the selected silica matrices (before and after PT) and corresponding carbon replicas were investigated by transmission electron microscopy imaging. The relevant micrographs are displayed in Fig. 6. The highly-ordered periodic 2D hexagonal *honeycomb* arrangement of the parent SBA-15 material and its carbon homologue CMK-3 with flat surface carbon nanorods of a truly cylindrical geometry is clearly seen (Fig. 6A, C). The structural features of SBA-15 were also preserved upon partial PT (Fig. 6B), however, in this case, the contrast between the regions of different densities is not so clearly pronounced as in the parent silica. The corresponding carbon

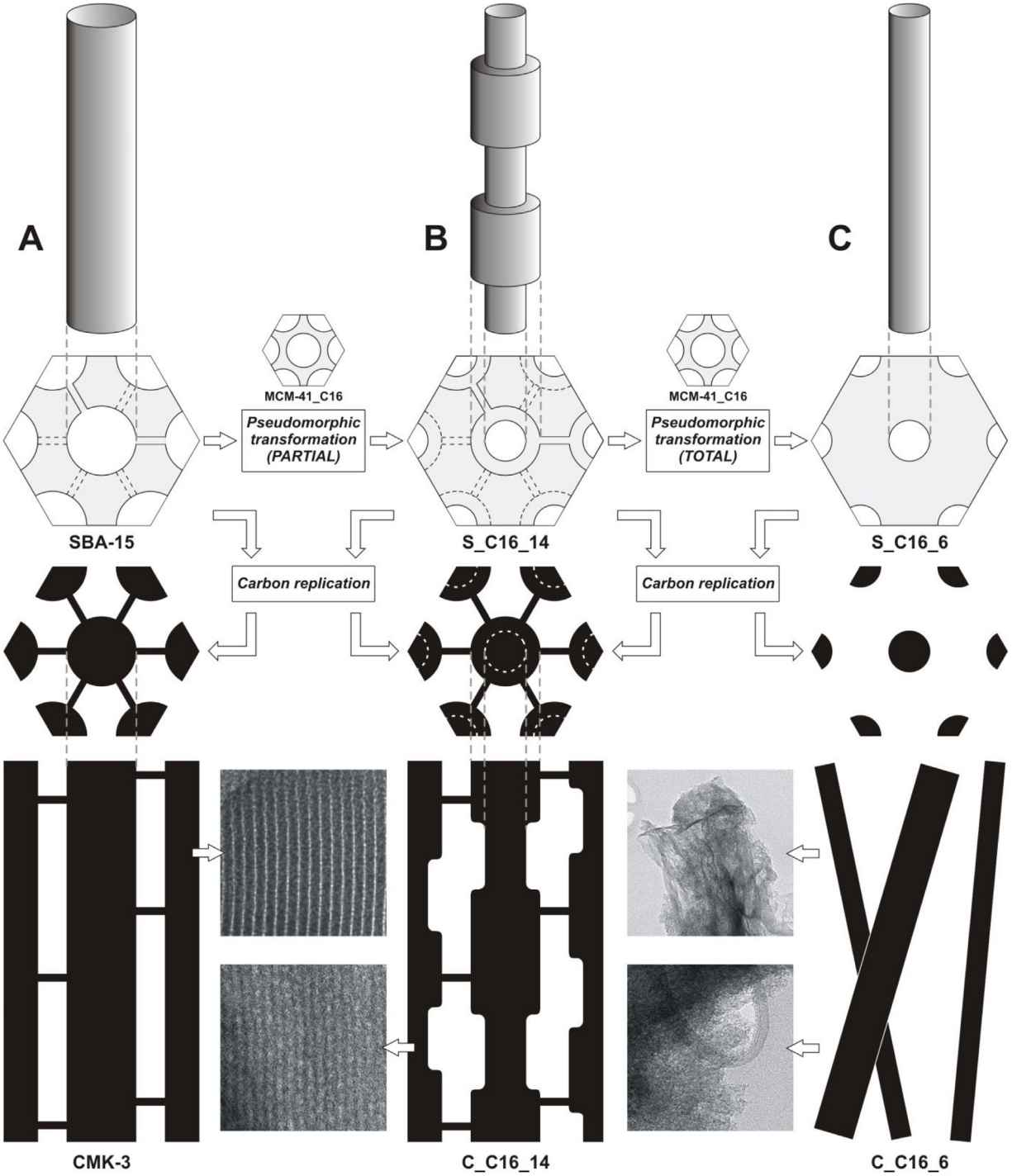

Fig. 8. Postulated pathway of the pseudomorphic transformation of SBA-15 into MCM-41 elucidated based on the study of negative structures of the carbon replicas obtained from SBA-15 (typical structure of CMK-3 replica) (A), SBA-15 partially transformed to MCM-41 (S_C16_14 – mixed SBA-15/MCM-41 with the *bottleneck* constrictions – CMK-3-like structure with the inverse *bottleneck* porosity) (B), and SBA-15 after total transformation to MCM-41 (S_C16_6 – lack of smaller interconnecting mesopores, the primary SBA-15 mesopores transformed to MCM-41 channels – collapse of the carbon replica structure) (C).

material exhibits similar character; also, in this case, the hexagonal array is evident (Fig. 6D). Interestingly, the micrographs taken longitudinally to the carbon rods show at a glance the presence of the aforementioned inhomogeneities in the diameter along the rod length (Fig. 6D inset; corrugations of carbon nanorods surface). The micrographs for the carbon replica obtained from the SBA-15 completely converted to the MCM-41-like material (Fig. 6E) reveal the total disintegration of the ordered framework. As seen, neither the *honeycomb* arrangement nor the morphology of the matrix particle were not preserved, suggesting the profound structure collapse, which is consistent with the foregoing discussion on the textural features.

We anticipated that it would be expedient to analyze the average particle size of the silicas and their carbon homologues. The volumetric particle size distributions computed from DLS measurements are gathered in Fig. 7.

The partial PT did not affect significantly the particle size (cf. Fig. 7A, B) — both intact SBA-15 and S_C16_14 silicas exhibit the particle size ranging within ca. 0.35–1.30 μm, however, a minor fraction of particles finer by an order of magnitude (ca. 0.05–0.12 μm) was found in the transformed material. This is probably due to the condensation of a part of dissolved silica (likely in the form of amorphous grains) outside the SBA-15 particle. The corresponding replicas show the particle sizes of 0.70–2.60 μm. This increase (with regard to the silicas) arises from the superficial deposition of the polymer shell onto matrix grain during the synthesis (cf. Section "Carbon nanoreplication: polymerization efficiency"). Contrarily, the carbon replica originated from SBA-15 after total PT shows a significant drop in the particle size down to 0.20–0.60 μm, which is comparable to that one of the MCM-41_C16-derived carbon (ca. 0.20–0.35 μm; Fig. 7C). The broader particle size distribution for the C_C16_6 carbon is understandable when considering the plausible formation of the carbon shell enveloping the particle. Nonetheless, the DLS measurements ultimately corroborate the disintegration of the C_C16_6 material after removal of the silica matrix revealed by XRD and TEM (Figs. 4C and 6 E, respectively). Noteworthy, this is a premise that tends us to rule out both *core–shell mechanism* of PT and its reverse variant.

Mechanism of pseudomorphic transformation of SBA-15 into MCM-41

The holistic consideration of the above results allows us to formulate a fundamental conclusion regarding the mechanism of SBA-15 transformation towards MCM-41-like structures. The sketch illustrating the postulated scenario of the partial and total PT of SBA-15 together with the drawings of the relevant carbon replicas with the TEM micrographs thereof are depicted in Fig. 8.

Fig. 8A presents the typical structure of SBA-15 drawn together with the corresponding CMK-3 carbon replica. As the pore arrangement of the pristine SBA-15 is reflected in its carbon analogue, the CMK-3 exhibits the structure built of carbon rods of a diameter of 6.1 nm (Table 3) that are merged themselves by narrower bridges, forming a highly ordered hexagonal skeleton. The structures of partially transformed SBA-15 (S_C16_14) and its carbon counterpart (C_C16_14) deduced from the structural and textural parameters are depicted in Fig. 8B. In this case, a mixed pore system constituted of larger channels originated from the SBA-15 accompanied by narrower MCM-41-like necks along a pore length is formed (Fig. 8B, top). Noteworthy, transverse narrower interconnecting mesopores originating from the intact SBA-15 were preserved. Consequently, the inverse carbon replica features the 2D hexagonal framework built of longitudinal bars with broader and narrower regions (resembling to some extent a *tube balloon* with its narrow and wider segments) (Fig. 8B, bottom). The irregular shape of these bars is clearly reflected in the nitrogen adsorption isotherm (relatively broad hysteresis loop), while the prominent total pore volume arises from the broader cavities present in the structure (Figs. 4A–b, c; 5 –b, c; Table 3). This clearly points to the PT proceeding homogeneously within the body of the silica grain. Thus, the dissolution of silica and its re-condensation around the micelles of SDA proceeds simultaneously throughout the entire particle's body, according to the anticipated *homogeneous transformation mechanism*.

Finally, in the case of total PT, the remaining SBA-15 pores undergo extinction; they are replaced by newly formed MCM-41-like channels (Fig. 8C, top). As a result, the structure shares common characteristics with typical MCM-41 (possessing a homogeneous, monomodal mesoporosity). The only difference is the wall thickness that is being vastly thicker (eightfold; Table 3) than for typical MCM-41. Obviously, as this material lost the channels interconnecting the main mesopores, its carbon replica undergoes collapse after removal of the silica matrix (Fig. 8C, bottom).

Conclusion

A series of mesoporous silicas with a combined bimodal SBA-15/MCM-41 porosity was synthesized by PT of SBA-15. The materials differed in both pore size of the MCM-41-like fraction and degree of PT. The mechanism of PT was for the first time investigated in a non-direct manner by the analysis of the structural and textural characteristics of the corresponding carbon replicas. It was found that the conversion of SBA-15 into MCM-41 proceeds simultaneously throughout the entire particle's body, according to the mechanism of *homogeneous pseudomorphic transformation*. Apparently, the inverse carbon replication can be successfully employed for studying structural and textural alterations of SiO_2, which occur along with the progress of PT. Thus, we have shown that nanoreplication may find a new application as an ingenious tool for studying hierarchically mesoporous materials. To the best of our knowledge, such approach was not reported as far in the literature.

The peculiar structures of both bimodal silicas and related carbons create an excellent opportunity for their application in modeling of diffusion and adsorption in porous solids. Besides, they may serve as superb candidates for *size-exclusion* membrane separation processes as well as in advanced catalytic processes, for instance, in so-called *ship in a bottle* reactions. Finally, the prominent pore volume of the produced carbon replicas (0.8–1.1 $cm^3 g^{-1}$) and developed specific surface area (1000–1175 $m^2 g^{-1}$) open up a way to utilizing them in a variety of applications in which materials featuring a subtle, openwork pore structure are desired, i.e. adsorption and catalysis. Besides, the carbon replicas may be used as templates for the synthesis of new mesostructured inorganic materials following the secondary nanocasting strategy.

Declaration of Competing Interest

The authors report no declarations of interest.

Acknowledgements

The research was carried out using the infrastructure of the AGH Centre of Energy, AGH University of Science and Technology as well as the Faculty of Chemistry, Jagiellonian University in Kraków. The latter one was partially purchased thanks to the financial support of the European Regional Development Fund in the framework of the Polish Innovation Economy Operational Program (Contract No. POIG.02.01.00-12-023/08). Dr. Jacek Jagiello (Micromeritics Instrument Corporation) is gratefully acknowledged for his valuable hints in terms of calculations of the textural parameters. Rafał Janus wishes to thank the AGH University of

Science and Technology for the financial support under the grant no. 15.11.210.409/2018.

Appendix A. Supplementary data

Supplementary material related to this article can be found, in the online version, at doi:https://doi.org/10.1016/j.jiec.2020.08.032.

References

[1] V. Chiola, J.E. Ritsko, C.D. Vanderpool. Process for producing low-bulk density silica. U.S. Patent 3,556,725, January 19, 1971.
[2] F. Di Renzo, H. Cambon, R. Dutartre, Microporous Mater. 10 (1997) 283, doi:http://dx.doi.org/10.1016/S0927-6513(97)00028-X.
[3] J.S. Beck. Method for synthesizing mesoporous crystalline material. U.S. Patent 5,057,296, October, 15, 1991.
[4] J.S. Beck, C.T-W. Chu, I.D. Johnson, C.T. Kresge, M.E. Leonowicz, W.J. Roth, J.C. Vartuli. Synthesis of mesoporous crystalline material. U.S. Patent 5,108,725, April 28, 1992.
[5] J.S. Beck, J.C. Vartuli, W.J. Roth, M.E. Leonowicz, C.T. Kresge, K.D. Schmitt, C.T.-W. Chu, D.H. Olson, E.W. Sheppard, S.B. McCullen, J.B. Higgins, J.L. Schlenker, J. Am. Chem. Soc. 114 (1992) 10834, doi:http://dx.doi.org/10.1021/ja00053a020.
[6] C.T. Kresge, M.E. Leonowicz, W.J. Roth, J.C. Vartuli, J.S. Beck, Nature 359 (1992) 710, doi:http://dx.doi.org/10.1038/359710a0.
[7] J.S. Beck, J.C. Vartuli, G.J. Kennedy, C.T. Kresge, W.J. Roth, S.E. Schramm, Chem. Mater. 6 (1994) 1816, doi:http://dx.doi.org/10.1021/cm00046a040.
[8] W.J. Roth. Synthesis of the cubic mesoporous molecular sieve MCM-48. U.S. Patent 6,096,288, August 1, 2000.
[9] D. Zhao, J. Feng, Q. Huo, N. Melosh, G.H. Fredrickson, B.F. Chmelka, G.D. Stucky, Science 279 (1998) 548, doi:http://dx.doi.org/10.1126/science.279.5350.548.
[10] Y. Wan, D. Zhao, Chem. Rev. 107 (2006) 2821, doi:http://dx.doi.org/10.1021/cr068020s.
[11] W. Wang, C. Wu, R. Sun, D. Li, H. Ru, Microporous Mesoporous Mater. 302 (2020) 110211, doi:http://dx.doi.org/10.1016/j.micromeso.2020.110211.
[12] C.C. Chong, Y.W. Cheng, S.N. Bukhari, H.D. Setiabudi, A.A. Jalil, Catal. Today (2020), doi:http://dx.doi.org/10.1016/j.cattod.2020.06.073 (in Press).
[13] C.C. Chong, S.N. Bukhari, Y.W. Cheng, H.D. Setiabudi, L.P. Teh, A.A. Jalil, Microporous Mesoporous Mater. 294 (2020) 109872, doi:http://dx.doi.org/10.1016/j.micromeso.2019.109872.
[14] R. Huirache-Acuña, R. Nava, C.L. Peza-Ledesma, J. Lara-Romero, G. Alonso-Núñez, B. Pawelec, E.M. Rivera-Muñoz, Materials 6 (2013) 4139, doi:http://dx.doi.org/10.3390/ma6094139.
[15] Z.A. Alothman, Materials 5 (2012) 2874, doi:http://dx.doi.org/10.3390/ma5122874.
[16] N. Rahmat, A.Z. Abdullah, A.R. Mohamed, Am. J. Appl. Sci. 7 (2010) 1579, doi:http://dx.doi.org/10.3844/ajassp.2010.1579.1586.
[17] S. Bhattacharyya, G. Lelong, M.L. Saboungi, J. Exp. Nanosci. 1 (2006) 375, doi:http://dx.doi.org/10.1080/17458080600812757.
[18] Q. Li, S.E. Brown, L.J. Broadbelt, J.G. Zheng, N.Q. Wu, Microporous Mesoporous Mater. 59 (2003) 105, doi:http://dx.doi.org/10.1016/S1387-1811(03)00290-7.
[19] P. Dai, T.T. Yan, X.X. Yu, Z.M. Bai, M.Z. Wu, Nanoscale Res. Lett. 11 (2016), doi:http://dx.doi.org/10.1186/s11671-016-1445-2.
[20] N.P. Hung, N.T.V. Hoan, N.V. Nghia, Nanosci. Nanotechnol. 3 (2013) 19, doi:http://dx.doi.org/10.5923/j.nn.20130301.04.
[21] A.K. Aboul-Gheit, S.M. Abdel-Hamid, S.A. Mahmoud, R.A. El-Salamony, J. Valyon, M.R. Mihályi, Á. Szegedi, J. Mater. Sci. 46 (2011) 3319, doi:http://dx.doi.org/10.1007/s10853-010-5219-4.
[22] H. Shankar, G. Rajasudha, A. Karthikeyan, V. Narayanan, A. Stephen, Nanotechnology 19 (2008) 315711, doi:http://dx.doi.org/10.1088/0957-4484/19/31/315711.
[23] X. Zhang, H. Dong, Y. Wang, N. Liu, Y. Zuo, L. Cui, Chem. Eng. J. 283 (2016) 1097, doi:http://dx.doi.org/10.1016/j.cej.2015.08.064.
[24] X. Zhang, H. Dong, Z. Gu, G. Wang, Y. Zuo, Y. Wang, L. Cui, Chem. Eng. J. 269 (2015) 94, doi:http://dx.doi.org/10.1016/j.cej.2015.01.085.
[25] Z. Wang, Q. Sun, D. Wang, Z. Hong, Z. Qu, X. Li, Sep. Purif. Technol. 209 (2019) 1016, doi:http://dx.doi.org/10.1016/j.seppur.2018.09.045.
[26] Y. Yang, F. Hou, H. Li, N. Liu, Y. Wang, X. Zhang, J. Porous Mater. 24 (2017) 1661, doi:http://dx.doi.org/10.1007/s10934-017-0406-1.
[27] H.J. Kim, H.C. Yang, D.Y. Chung, I.H. Yang, Y.J. Choi, J.K. Moon, J. Chem. (2015), doi:http://dx.doi.org/10.1155/2015/202867 Article ID 202867.
[28] E. Dündar-Tekkaya, Y. Yürüm, Int. J. Hydrogen Energy 41 (2016) 9789, doi:http://dx.doi.org/10.1016/j.ijhydene.2016.03.050.
[29] Y. Fu, Y. Huang, J. Hu, R. Soc. Open Sci. 5 (2018) 171927, doi:http://dx.doi.org/10.1098/rsos.171927.
[30] Y.Q. Yeh, C.Y. Tang, C.Y. Mou, APL Mater. 2 (2014) 113303, doi:http://dx.doi.org/10.1063/1.4897203.
[31] R. Janus, M. Wądrzyk, P. Natkański, P. Cool, P. Kuśtrowski, J. Ind. Eng. Chem. 71 (2019) 465, doi:http://dx.doi.org/10.1016/j.jiec.2018.12.004.
[32] R. Janus, A. Wach, P. Kuśtrowski, B. Dudek, M. Drozdek, A.M. Silvestre-Albero, F. Rodríguez-Reinoso, P. Cool, Langmuir 29 (2013) 3045, doi:http://dx.doi.org/10.1021/la3041852.
[33] R. Janus, P. Natkański, A. Wach, M. Drozdek, Z. Piwowarska, P. Cool, P. Kuśtrowski, J. Therm. Anal. Calorim. 110 (2012) 119, doi:http://dx.doi.org/10.1007/s10973-011-2157-6.
[34] K. Machowski, P. Natkański, A. Białas, P. Kuśtrowski, J. Therm. Anal. Calorim. 126 (2016) 1313, doi:http://dx.doi.org/10.1007/s10973-016-5614-4.
[35] P. Kuśtrowski, R. Janus, A. Kochanowski, L. Chmielarz, B. Dudek, Z. Piwowarska, M. Michalik, Mater. Res. Bull. 45 (2010) 787, doi:http://dx.doi.org/10.1016/j.materresbull.2010.03.017.
[36] T. Martin, A. Galarneau, F. Di Renzo, D. Brunel, F. Fajula, S. Heinisch, G. Crétier, J. L. Rocca, Chem. Mater. 16 (2004) 1725, doi:http://dx.doi.org/10.1021/cm030443c.
[37] M. Raimondo, G. Perez, M. Sinibaldi, A. De Stefanis, A.A.G. Tomlinson, Chem. Commun. (1997) 1343, doi:http://dx.doi.org/10.1039/a702849k.
[38] M. Grün, A.A. Kurganov, S. Schacht, F. Schüth, K.K. Unger, J. Chromatogr. A 740 (1996) 1, doi:http://dx.doi.org/10.1016/0021-9673(96)00205-1.
[39] J. Zhao, F. Gao, Y. Fu, W. Jin, P. Yang, D. Zhao, Chem. Commun. 7 (2002) 752, doi:http://dx.doi.org/10.1039/B110637F.
[40] N. Calin, A. Galarneau, T. Cacciaguerra, R. Denoyel, F. Fajula, C.R. Chim. 13 (2010) 199, doi:http://dx.doi.org/10.1016/j.crci.2009.04.001.
[41] S. Wang, Microporous Mesoporous Mater. 117 (2009) 1, doi:http://dx.doi.org/10.1016/j.micromeso.2008.07.002.
[42] W. Xu, J. Riikonen, V.P. Lehto, Int. J. Pharm. 453 (2013) 181, doi:http://dx.doi.org/10.1016/j.ijpharm.2012.09.008.
[43] R.A. Jesus, A.S. Rabelo, R.T. Figueiredo, L.C. Cides da Silva, I.C. Codentino, M.C.A. Fantini, G.L.B. Araújo, A.A.S. Araújo, M.E. Mesquita, J. Drug Delivery Sci. Technol. 31 (2016) 153, doi:http://dx.doi.org/10.1016/j.jddst.2015.11.008.
[44] C.A. Stewart, Y. Finer, B.D. Hatton, Sci. Rep. 8 (2018), doi:http://dx.doi.org/10.1038/s41598-018-19166-8.
[45] M. Martínez-Carmona, Y.K. Gun'ko, M. Vallet-Regí, Pharmaceutics 10 (2018) 279, doi:http://dx.doi.org/10.3390/pharmaceutics10040279.
[46] G. Martínez-Edo, A. Balmori, I. Pontón, A. Martí del Rio, D. Sánchez-García, Catalysts 8 (2018) 617, doi:http://dx.doi.org/10.3390/catal8120617.
[47] J. Gao, Y. Jiang, J. Lu, Z. Han, J. Deng, Y. Chen, Sci. Rep. 7 (2017) 40395, doi:http://dx.doi.org/10.1038/srep40395.
[48] Z. Zhang, L. Zhang, C. Zhang, W. Zhang, Talanta 119 (2014) 485, doi:http://dx.doi.org/10.1016/j.talanta.2013.11.037.
[49] S. Li, Z. Wu, M. Lu, Z. Wang, Z. Li, Molecules 18 (2013) 1138, doi:http://dx.doi.org/10.3390/molecules18011138.
[50] T. Wagner, S. Haffer, C. Weinberger, D. Klaus, M. Tiemann, Chem. Soc. Rev. 42 (2013) 4036, doi:http://dx.doi.org/10.1039/c2cs35379b.
[51] B.J. Melde, B.J. Johnson, P.T. Charles, Sensors 8 (2008) 5202, doi:http://dx.doi.org/10.3390/s8085202.
[52] C.C. Yang, Y.R. Zheng, J. Power Sources 201 (2012) 387, doi:http://dx.doi.org/10.1016/j.jpowsour.2011.10.111.
[53] J. Zhi, S. Deng, Y. Zhang, Y. Wang, A. Hu, J. Mater. Chem. A 1 (2013) 3171, doi:http://dx.doi.org/10.1039/c2ta01253g.
[54] R. Ragavan, A. Pandurangan, New J. Chem. 41 (2017) 11591, doi:http://dx.doi.org/10.1039/c7nj00804j.
[55] A. Deryło-Marczewska, M. Zienkiewicz-Strzałka, K. Skrzypczyńska, A. Świątkowski, K. Kuśmierek, Adsorption 22 (2016) 801, doi:http://dx.doi.org/10.1007/s10450-016-9779-8.
[56] I. Cesarino, G. Marino, J. do Rosário Matos, É.T.G. Cavalheiro, Talanta 75 (2008) 15, doi:http://dx.doi.org/10.1016/j.talanta.2007.06.032.
[57] R. Ryoo, S.H. Joo, S. Jun, J. Phys. Chem. B 103 (1999) 7743, doi:http://dx.doi.org/10.1021/jp991673a.
[58] P. Janus, R. Janus, P. Kuśtrowski, S. Jarczewski, A. Wach, A.M. Silvestre-Albero, F. Rodríguez-Reinoso, Catal. Today 235 (2014) 201, doi:http://dx.doi.org/10.1016/j.cattod.2014.03.019.
[59] P. Kuśtrowski, R. Janus, P. Niebrzydowska. Method of synthesis of CMK-3-type carbon replica. U.S. Patent 9,302,252 B2, April 5, 2016.
[60] R. Janus, P. Natkański, M. Wądrzyk, B. Dudek, M. Gajewska, P. Kuśtrowski, Mater. Today Commun. 13 (2017) 6, doi:http://dx.doi.org/10.1016/j.mtcomm.2017.07.009.
[61] M. Kruk, M. Jaroniec, R. Ryoo, S.H. Joo, J. Phys. Chem. B 104 (2000) 7960, doi:http://dx.doi.org/10.1021/jp000861u.
[62] J.Y. Kim, S.B. Yoon, F. Kooli, J.S. Yu, J. Mater. Chem. 11 (2001) 2912, doi:http://dx.doi.org/10.1039/b108207h.
[63] X. Deng, K. Chen, H. Tüysüz, Chem. Mater. 29 (2017) 40, doi:http://dx.doi.org/10.1021/acs.chemmater.6b02645.
[64] J. Roggenbuck, G. Koch, M. Tiemann, Chem. Mater. 18 (2006) 4151, doi:http://dx.doi.org/10.1021/cm060740s.
[65] D. Gu, F. Schüth, Chem. Soc. Rev. 43 (2014) 313, doi:http://dx.doi.org/10.1039/c3cs60155b.
[66] T. Martin, A. Galarneau, F. Di Renzo, F. Fajula, D. Plee, Angew. Chem. Int. Ed. 41 (2002) 2590, doi:http://dx.doi.org/10.1002/1521-3757(20020715)114:14%3C2702::AID-ANGE2702%3E3.0.CO;2-%23.
[67] B. Lefèvre, A. Galarneau, J. Iapichella, C. Petitto, F. Di Renzo, F. Fajula, Z. Bayram-Hahn, R. Skudas, K. Unger, Chem. Mater. 17 (2005) 601, doi:http://dx.doi.org/10.1021/cm048481z.
[68] C. Petitto, A. Galarneau, M.F. Driole, B. Chiche, B. Alonso, F. Di Renzo, F. Fajula, Chem. Mater. 17 (2005) 2120, doi:http://dx.doi.org/10.1021/cm050068j.
[69] A. Galarneau, J. Iapichella, K. Bonhomme, F. Di Renzo, P. Kooyman, O. Terasaki, F. Fajula, Adv. Funct. Mater. 16 (2006) 1657, doi:http://dx.doi.org/10.1002/adfm.200500825.
[70] M.J. Reber, D. Brühwiler, Dalton Trans. 44 (2015) 17960, doi:http://dx.doi.org/10.1039/c5dt03082j.

[71] A. Galarneau, A. Sachse, B. Said, C.H. Pelisson, P. Boscaro, N. Brun, L. Courtheoux, N. Olivi-Tran, B. Coasne, F. Fajula, C.R. Chim. 19 (2016) 231, doi:http://dx.doi.org/10.1016/j.crci.2015.05.017.
[72] H. Uhlig, J. Hollenbach, M. Rogaczewski, J. Matysik, F.J. Brieler, M. Fröba, D. Enke, Chem. Ing. Tech. 89 (2017) 863, doi:http://dx.doi.org/10.1002/cite.201600189.
[73] W.D. Einicke, D. Enke, M. Dvoyashkin, R. Valiullin, R. Gläser, Materials 6 (2013) 3688, doi:http://dx.doi.org/10.3390/ma6093688.
[74] N. Zucchetto, M.J. Reber, L. Pestalozzi, R. Schmid, A. Neels, D. Brühwiler, Microporous Mesoporous Mater. 257 (2018) 232, doi:http://dx.doi.org/10.1016/j.micromeso.2017.08.046.
[75] M.J. Reber, D. Brühwiler, Part. Part. Syst. Charact. 32 (2015) 243, doi:http://dx.doi.org/10.1002/ppsc.201400150.
[76] Y. Xia, R. Mokaya, J. Mater. Chem. 13 (2003) 3112, doi:http://dx.doi.org/10.1039/b305404g.
[77] P. Niebrzydowska, R. Janus, P. Kuśtrowski, S. Jarczewski, A. Wach, A.M. Silvestre-Albero, F. Rodríguez-Reinoso, Carbon 64 (2013) 252, doi:http://dx.doi.org/10.1016/j.carbon.2013.07.060.
[78] P. Janus, R. Janus, B. Dudek, M. Drozdek, A. Silvestre-Albero, F. Rodríguez-Reinoso, P. Kuśtrowski, Microporous Mesoporous Mater. 299 (2020) 110118, doi:http://dx.doi.org/10.1016/j.micromeso.2020.110118.
[79] M. Kruk, M. Jaroniec, S.H. Joo, R. Ryoo, J. Phys. Chem. B 107 (2003) 2205, doi:http://dx.doi.org/10.1021/jp0271514.
[80] R. Janus, P. Kuśtrowski, B. Dudek, Z. Piwowarska, A. Kochanowski, M. Michalik, P. Cool, Microporous Mesoporous Mater. 145 (2011) 65, doi:http://dx.doi.org/10.1016/j.micromeso.2011.04.029.
[81] M. Thommes, K. Kaneko, A.V. Neimark, J.P. Olivier, F. Rodríguez-Reinoso, J. Rouquerol, K.S.W. Sing, Pure Appl. Chem. 87 (2015) 1051, doi:http://dx.doi.org/10.1515/pac-2014-1117.
[82] K.A. Cychosz, R. Guillet-Nicolas, J. García-Martínez, M. Thommes, Chem. Soc. Rev. 46 (2017) 389, doi:http://dx.doi.org/10.1039/c6cs00391e.
[83] M. Jaroniec, M. Kruk, J.P. Olivier, Langmuir 15 (1999) 5410, doi:http://dx.doi.org/10.1021/la990136e.
[84] A. Silvestre-Albero, J. Silvestre-Albero, M. Martínez-Escandell, R. Futamura, T. Itoh, K. Kaneko, F. Rodríguez-Reinoso, Carbon 66 (2014) 699, doi:http://dx.doi.org/10.1016/j.carbon.2013.09.068.
[85] F. Rouquerol, J. Rouquerol, K.S.W. Sing, P. Llewellyn, G. Maurin, Adsorption by Powders and Porous Solids: Principles, Methodology and Applications, second edition, (2014), doi:http://dx.doi.org/10.1016/B978-0-08-097035-6.00007-3 p. 237.
[86] M. Thommes, K.A. Cychosz, A.V. Neimark, in: J.M.D. Tascón (Ed.), Advanced Physical Adsorption Characterization of Nanoporous Carbons. Novel Carbon Adsorbents, Elsevier Ltd., 2012, doi:http://dx.doi.org/10.1016/b978-0-08-097744-7.00004-1 p. 107.
[87] J. Landers, G.Y. Gor, A.V. Neimark, Colloids Surf. A 437 (2013) 3, doi:http://dx.doi.org/10.1016/j.colsurfa.2013.01.007.
[88] J. Jagiello, J.P. Olivier, Carbon 55 (2013) 70, doi:http://dx.doi.org/10.1016/j.carbon.2012.12.011.
[89] J. Jagiello, J.P. Olivier, Adsorption 19 (2013) 777, doi:http://dx.doi.org/10.1007/s10450-013-9517-4.
[90] M. Kruk, M. Jaroniec, A. Sayari, Langmuir 13 (1997) 6267, doi:http://dx.doi.org/10.1021/la970776m.
[91] S.H. Joo, R. Ryoo, M. Kruk, M. Jaroniec, J. Phys. Chem. B 106 (2002) 4640, doi:http://dx.doi.org/10.1021/jp013583n.